Heterogeneous nanometer-scale Joule and Peltier effects in sub-25 nm thin phase change memory devices

Kyle L. Grosse,[1] Eric Pop,[2] and William P. King[1,3,a)]
[1]*Deptartment of Mechanical Science & Engineering, University of Illinois at Urbana-Champaign, Urbana, Illinois 61801, USA*
[2]*Department of Electrical Engineering, Stanford University, Stanford, California 94305, USA*
[3]*Department of Materials Science and Engineering and Materials Research Laboratory, University of Illinois at Urbana-Champaign, Urbana, Illinois 61801, USA*

(Received 6 May 2014; accepted 14 September 2014; published online 24 September 2014)

We measure heterogeneous power dissipation in phase change memory (PCM) films of 11 and 22 nm thin $Ge_2Sb_2Te_5$ (GST) by scanning Joule expansion microscopy (SJEM), with sub-50 nm spatial and ~0.2 K temperature resolution. The heterogeneous Joule and Peltier effects are explained using a finite element analysis (FEA) model with a mixture of hexagonal close-packed and face-centered cubic GST phases. Transfer length method measurements and effective media theory calculations yield the GST resistivity, GST-TiW contact resistivity, and crystal fraction of the GST films at different annealing temperatures. Further comparison of SJEM measurements and FEA modeling also predicts the thermopower of thin GST films. These measurements of nanometer-scale Joule, thermoelectric, and interface effects in PCM films could lead to energy-efficient designs of highly scaled PCM technology. © *2014 AIP Publishing LLC*.
[http://dx.doi.org/10.1063/1.4896492]

I. INTRODUCTION

Phase change memory[1] (PCM) is a non-volatile memory technology with potential for fast (sub-nanosecond)[2] and low power (femtojoule)[3,4] operation. PCM has potential to replace DRAM and Flash memory in future electronics.[5] Data in chalcogenide based PCM, such as $Ge_2Sb_2Te_5$ (GST), are stored by the large ratio ($>10^3$) in electrical resistance between amorphous and crystalline states of the material. Reversible switching between phases is typically driven by Joule heating; however, Peltier,[6] Seebeck,[7] and Thomson[8] effects have been observed to contribute to phase change.[9] Previous studies have shown that the thermopower for bulk and thin film face-centered cubic (fcc) GST is large (200–400 μV K^{-1}).[7,10–13] Higher temperature annealing forms hexagonal close-packed (hcp) GST[14] which reduces the GST thermopower (15–50 μV K^{-1}).[7,10,11,13] Few studies have examined the effect of amorphous, fcc, and hcp phases on electrical[15,16] or thermoelectric[7,12] properties of thin GST films, which are important for device scaling. Electrical contacts and thermal interfaces to GST are also important for heat generation and thermal confinement of GST devices.[17–20] Recent work has measured the role of interfaces[17] and thermoelectric effects[6,8,12] in GST devices. These studies are essential, since electrical and thermal interfaces could reduce PCM programming power[17,18] by 20%–30%, and thermoelectric effects may reduce power consumption[9] an additional 20%–40% depending on the thermopower of thin GST films. However, little is known of electrical properties, interface resistances, thermopower, and heat generation in sub-25 nm thin GST films.

In this study, we measured the nanometer-scale temperature distribution and properties of lateral PCM devices with 11 and 22 nm thin GST. Transfer length method (TLM) measurements on devices with varying channel lengths yielded the GST electrical resistivity ρ_{GST} and GST-TiW contact resistivity ρ_C for each sample. Effective media theory (EMT)[7,21] calculations yielded the crystal fraction of amorphous, fcc, and hcp GST for the 11 and 22 nm thin GST samples annealed at 150, 200, and 250 °C. Nanometer-scale thermometry with sub-50 nm spatial and ~0.2 K temperature resolution was accomplished by scanning Joule expansion microscopy (SJEM),[12,22–25,35] an atomic force microscopy (AFM) based technique. The SJEM technique is modified for simultaneous and direct observation of Joule and Peltier effects on working PCM devices. We observe *uniform* heating for mixed amorphous and fcc GST thin films, and laterally *heterogeneous* Joule and thermoelectric effects in mixed fcc and hcp GST thin films. Increasing the annealing temperature increases the hcp GST crystal fraction and the heterogenous Joule heating and Peltier heating and cooling between fcc and hcp GST. We develop a two and three dimensional (2D and 3D) finite element analysis (FEA) model to understand SJEM results. The 3D FEA model predicts the observed heterogeneous heating and estimates the hcp GST grain size. Comparing SJEM measurements with the 2D FEA model predicts ρ_{GST} and ρ_C, which are in good agreement with values obtained from TLM measurements. The good agreement between TLM measurements and FEA fitting of SJEM measurements to predict the properties of the sub-25 nm thin GST films indicates both methods are accurate for measuring device properties. SJEM measurements and modeling also yield the first measurements of the thermopower of sub-25 nm thin GST films.

a)Author to whom correspondence should be addressed. Electronic mail: wpk@illinois.edu

II. MEASUREMENTS

A. Device fabrication and SJEM measurements

Figure 1(a) shows the lateral GST device. A 300 nm SiO_2/Si wafer was diced into $\sim 1.5 \times 1.5\,cm^2$ samples, and GST with thickness $t_{GST} = 11$ or 22 nm was sputtered onto the samples at 5 mT in an Ar environment at a rate of 2.5 nm min^{-1}. The samples were annealed at a temperature $T_A = 150$, 200, or 250 °C for 10 min in a N_2 environment, with a heating and cooling rate of $\sim 30\,°C\ min^{-1}$. The supplement describes *in-situ* two probe measurements of the sample resistance while annealing.[26] After annealing, lateral GST devices with channel length $L = 2$ to 12 μm were fabricated by photolithography patterning and sputtering of 10 nm TiW (10/90% weight) and 30–60 nm Au. The Au reduces the electrode sheet resistance. Fabrication was completed by spin coating 60–200 nm of poly(methyl methacrylate) (PMMA) on the samples. The PMMA serves a dual purpose: it protects the devices from oxidation, and amplifies thermo-mechanical expansions of the PCM device during operation.[12]

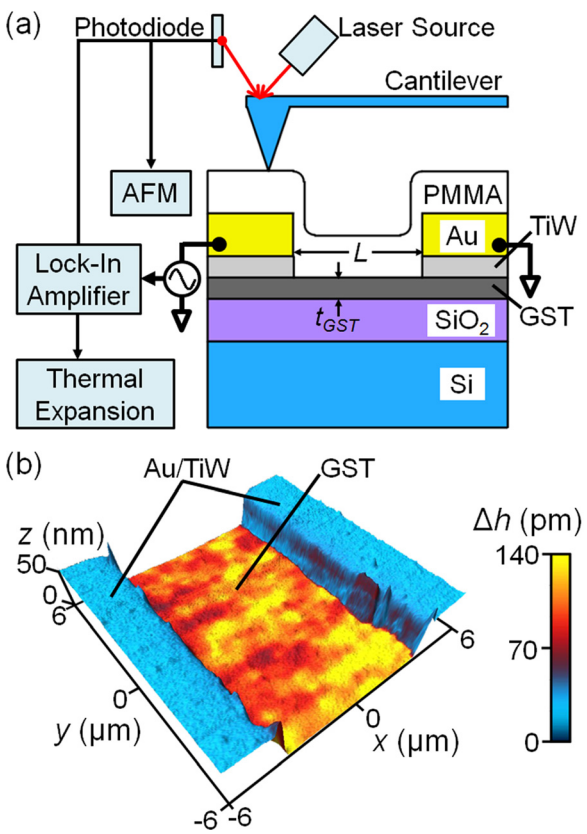

FIG. 1. (a) Schematic of lateral PCM device and SJEM. PCM devices consisted of 60-200 nm of PMMA, 30–60 nm of Au, 10 nm TiW, 11–22 nm GST, and 300 nm SiO_2 on a Si substrate, from top to bottom. The device channel length and GST thickness are shown by L and t_{GST}. SJEM operates by supplying a periodic voltage waveform to resistively heat the device while the AFM measures the resulting peak-to-peak surface thermo-mechanical expansion Δh. (b) Measured Δh overlaid on topography for device with channel length 7.5 μm, GST thickness 22 nm, and anneal temperature 250 °C. The peak-to-peak temperature rise ΔT is proportional to the measured Δh.[12,22,25] The measured thermo-mechanical expansion is non-uniform indicating heterogeneous lateral GST structure.

Figure 1(a) shows a schematic of the SJEM experiment. A sinusoidal waveform at frequency $\omega = 43$ kHz and bias amplitude V drives the device and generates resistive heating within the device. The periodic resistive heating of the device locally increases the temperature of the surrounding PMMA, SiO_2, and Si substrate. The resulting thermo-mechanical expansions of the sample were measured by the AFM laser, photodiode, and cantilever in contact with the surface. A lock-in amplifier at the first or second harmonic, 1ω or 2ω, with a low-pass filter bandwidth of 3–27 Hz recorded the peak-to-peak (twice the amplitude) surface expansion Δh down to $\sim$2–3 pm. The measurement spatial resolution was $\sim$50 nm and temperature resolution was $\sim$0.2 K.[12,22] SJEM can resolve current crowding and Peltier effects due to current flow between the GST and TiW as the current transfer length $L_T = 0.4$–1.2 μm between the GST-TiW (the distance over which $1/e$ of the current is transferred between the two materials) is greater than the spatial resolution.[12]

A FEA model was used to interpret the SJEM measurements by predicting the thermo-mechanical surface expansion and corresponding GST temperature rise. The model simulates Joule and thermoelectric effects in the GST device using modified heat diffusion and Poisson equations.[27,28] To simulate the SJEM measurements, the predicted temperature field was coupled with a thermo-mechanical model. The Fourier transform of the equations yielded the frequency response of the predicted Δh and ΔT.[12] The supplement contains additional information on the model.[26]

Figure 1(b) shows the measured surface expansion Δh overlaid on the topography of a 7.5 μm channel length and 22 nm thin GST device annealed at 250 °C. The device was biased with $V_{DS} = 8.9$ V. Subtracting the voltage drop across the electrodes and probes from V yields the device bias amplitude V_{DS}. The GST peak-to-peak temperature rise ΔT is proportional to Δh and is related using FEA modeling.[12,22,25] The measured Δh is non-uniform across the device, indicating heterogeneous lateral heating, electric field, and resistivity distribution due to the presence of mixed fcc and hcp GST.

Figure 2 shows how SJEM can measure both Joule and Peltier effects. Figure 2(a) shows a simple diagram of the lateral GST devices, where hole flow into (from) the contacts locally heats (cools) the device.[12,22,29] The schematic shows both time and frequency domain diagrams of the technique. We distinguish the time dependent device bias $V_{DS}(t)$ from the frequency domain zero and first harmonic device bias by $V_{DS,0\omega}$ and $V_{DS,1\omega}$, where $V_{DS,1\omega}$ is a complex number. We distinguish the time dependent temperature rise T from the zero, first, and second harmonic temperature rise by $T_{0\omega}$, $T_{1\omega}$, and $T_{2\omega}$, where $T_{1\omega}$ and $T_{2\omega}$ are complex numbers. The first and second harmonic peak-to-peak temperature rise are given by $\Delta T_{1\omega} = 2|T_{1\omega}|$ and $\Delta T_{2\omega} = 2|T_{2\omega}|$. For SJEM measurements, the peak-to-peak device temperature rise ΔT is proportional to the measured peak-to-peak sample surface thermo-mechanical expansion Δh.

Figure 2(b) shows the temperature distribution for a bipolar waveform, defined as $V_{DS}(t) = V_{DS,1\omega}\sin(2\pi\omega t)$ where time is given by t. Joule heating is evident as the large temperature rise across the device and is independent of the

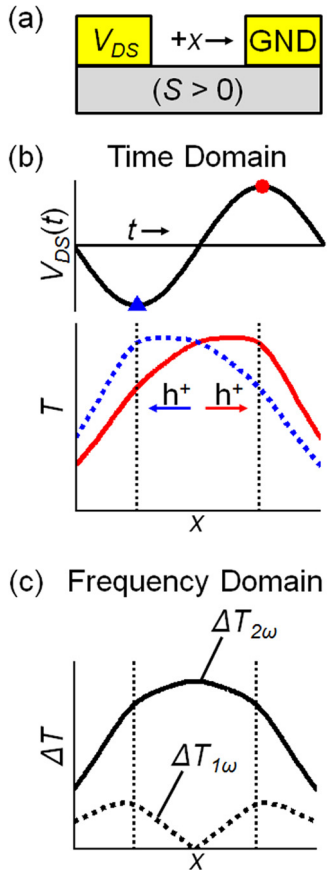

FIG 2. Diagram of direct SJEM observations of Joule and Peltier effects. (a) Schematic of device with two electrodes on a positive thermopower ($S > 0$) channel, similar to the lateral GST devices. The left and right electrodes are biased at V_{DS} and ground (GND) and have $S = 0$. (b) Time domain diagram of $V_{DS}(t)$ and the device temperature rise T. Top image shows V_{DS} in time t for a bipolar waveform, and the bottom image shows T in red solid and blue dashed lines corresponding to V_{DS} for the red circle and blue triangle in the top image. (c) The resultant frequency domain first and second harmonic temperature rise $\Delta T_{1\omega}$ and $\Delta T_{2\omega}$ in dashed and solid black lines. Joule and Peltier effects are proportional to $\Delta T_{2\omega}$ and $\Delta T_{1\omega}$. The vertical dashed black lines indicate the channel edges.

carrier flow direction. The Peltier effect is evident at the contacts as the small change in T with carrier flow direction.[12,22] Joule heating is proportional to V_{DS}^2 and Peltier effects are proportional to V_{DS}. Joule heating occurs at the zero and second harmonic 2ω, and Peltier effects occur at the first harmonic 1ω for a device subject to a bipolar waveform. Therefore, $\Delta T_{2\omega}$ is due to Joule heating, and $\Delta T_{1\omega}$ is due to Peltier effects. Figure 2(c) shows the frequency domain $\Delta T_{1\omega}$ and $\Delta T_{2\omega}$ from Fig. 2(b). Joule heating is evident in Fig. 2(c) as the large $\Delta T_{2\omega}$ across the channel. Peltier effects are evident as the small $\Delta T_{1\omega}$ at the contacts. Thus, SJEM provides independant measurements of Joule and Peltier effects.[35] We note $T_{1\omega}$ experiences a 180° phase shift between the contacts as Peltier heating or cooling of the contacts depends on the bias polarity, or carrier flow direction.[12,22]

B. GST properties

TLM measurements were used to obtain device and contact resistance for each sample. The lateral GST devices have a device width $W = 245\,\mu$m and source-drain spacing $L = 2$–$12\,\mu$m. The sheet and contact resistance of each sample was calculated from simple linear regression of the measured resistance of more than 10 devices per sample. The GST resistivity, GST-TiW contact resistivity, and current transfer length were calculated from the sheet and contact resistance.[12,22,30] The supplement shows the TLM measurements and analysis.[26]

Figure 3(a) shows the GST resistivity and GST-TiW contact resistivity from TLM measurements on all the samples. The measured GST resistivity ρ_{GST} continuously decreases with increasing annealing temperature. The measured GST-TiW contact resistivity ρ_C also decreases with annealing temperature until $T_A = 250\,^\circ$C. The contact resistance for the samples annealed at 250 °C is a few ohms, near our TLM measurement resolution, and we are unable to determine if ρ_C is lower than the values shown in Fig. 3(a) from TLM measurements. The measured contact resistance of the 22 nm thin GST sample annealed at 200 °C is also near the measurement resolution.

EMT[21] was applied to calculate the crystal fraction x_f of the GST phases[7] of each sample. The *in-situ* annealing resistance measurements[26] show a large ($\sim 10^3$–$10^4\ \Omega$) change in sample resistance at ~160 °C indicating the majority of GST quickly changes from amorphous to fcc GST.[31,32] The sample resistance continuously decreases with increased

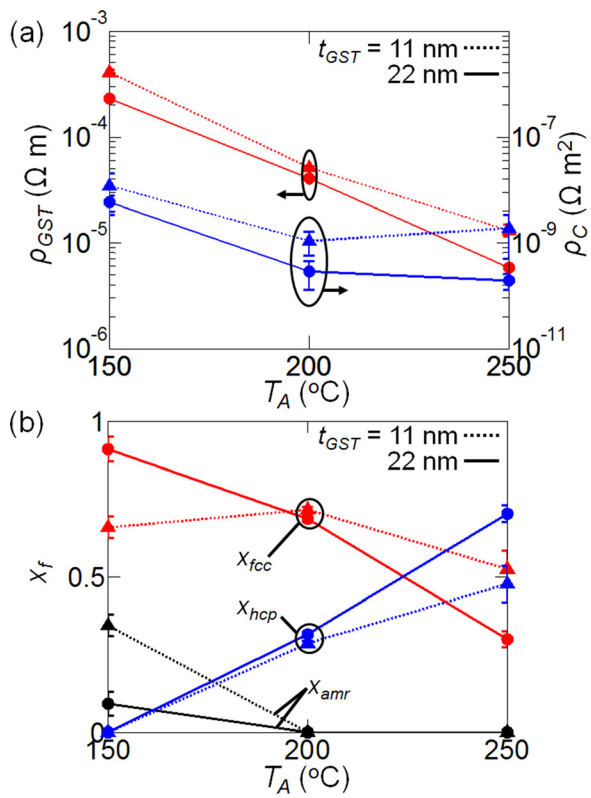

FIG. 3. (a) Calculated GST resistivity ρ_{GST} and GST-TiW contact resistivity ρ_C with annealing temperature T_A from TLM measurements. Red and blue lines show ρ_{GST} and ρ_C. (b) Calculated crystal fraction x_f from EMT[21] of amorphous, fcc, and hcp phase GST (x_{amr}, x_{fcc}, and x_{hcp}) are shown in black, red, and blue lines. The figure shows dotted lines with triangle markers and solid lines with circle markers for 11 and 22 nm thin GST.

annealing temperature indicating a gradual transition from fcc to hcp GST.[14] Samples annealed above 160 °C have little amorphous phase present and are assumed to be a binary mixture of fcc and hcp GST. Samples annealed below 160 °C have significant amorphous phase and are assumed to be a binary mixture of amorphous and fcc GST. The application of EMT is further described in the supplement.[26]

Figure 3(b) shows the calculated crystal fraction for amorphous, fcc, and hcp GST for each sample. The crystal fraction of amorphous, fcc, and hcp GST is given by x_{amr}, x_{fcc}, and x_{hcp}. The majority of samples are dominated by fcc GST; except the two samples annealed at 250 °C have a significant fraction of hcp GST. We are unable to explain the observed trends in the calculated crystal fraction with GST thickness. Previous work has shown the amorphous to fcc phase transition temperature does not significantly change with film thickness and the fcc to hcp transition temperature decreases with decreasing film thickness.[32] Therefore, we expect similar x_f for samples annealed at 150 °C and higher x_{hcp} for the thinner samples annealed at higher temperatures, contrary to our observations. Interfaces dominate the growth kinetics of thin film GST,[31] and further work is required to understand the growth of thin GST films on SiO_2.

III. RESULTS AND DISCUSSION

A. SJEM measurements of uniform GST devices

Figure 4 shows the measured and predicted Δh for 2.2 μm channel length and 22 nm thin GST device annealed at 200 °C. The device is biased with amplitude $V_{DS} = 0.9$, 1.2, and 1.5 V. The measured Δh was uniform in the y-direction indicating uniform lateral heating, electric field, and resistivity distribution. Comparison of measurements and predictions of the surface expansion and temperature distribution in the device yields the GST properties.[12] Measurements are an average of 18 line scans with deviation smaller than the markers.

Figure 4 shows measurements and predictions of Joule heating, current crowding, and Peltier effects. Figure 4(a) shows the measured and predicted $\Delta h_{2\omega}$, due to Joule heating. Joule heating occurs in the GST channel and at the GST-TiW contacts due to finite ρ_{GST} and ρ_C.[12,22] Fitting the measured and predicted $\Delta h_{2\omega}$ predicts $\rho_{GST} = 4.8 \pm 0.3 \times 10^{-5}$ Ω m and $\rho_C = 1.1 \pm 0.3 \times 10^{-11}$ Ω m^2 for the 2.2 μm channel length and 22 nm thin GST device annealed at 200 °C, similar to TLM measurements. Figure 4(b) shows the predicted $\Delta T_{2\omega}$ from Fig. 4(a). The predicted $\Delta T_{2\omega}$ is larger than our previous measurements for thin GST films.[12] Figure 4(c) shows the measured and predicted $\Delta h_{1\omega}$, due to Peltier effects. Peltier heating and cooling occurs at the GST-TiW contact due to their difference in thermopower.[12,22,29] Fitting the measured and predicted $\Delta h_{1\omega}$ yields $S_{GST} = 110 \pm 10\,\mu$V K^{-1} for the device with a calculated composition of 69 ± 1% fcc and 31 ± 1% hcp GST. Fitting measurements and predictions for ρ_{GST}, ρ_C, and S_{GST} yields a coefficient of determination $R^2 = 0.68$ between FEA predictions and SJEM measurements. The fitting error was determined by fitting each measured line scan to FEA predictions. Although the coefficient of determination is low for fitting FEA predictions to SJEM measurements, the predicted GST properties are in agreement with TLM measurements, indicating the FEA model accurately predicts the GST properties and device temperature rise. A small spike in $\Delta h_{1\omega}$ is observed at $x = 0$ μm, due to the presence of a small grain of hcp GST in the predominately fcc GST sample. The difference in S_{GST} between fcc and hcp GST causes local Peltier effects in the channel, explored further below, and was not included in 2D FEA simulations. Figure 4(d) shows the predicted $\Delta T_{1\omega}$ from Fig. 4(c). At the

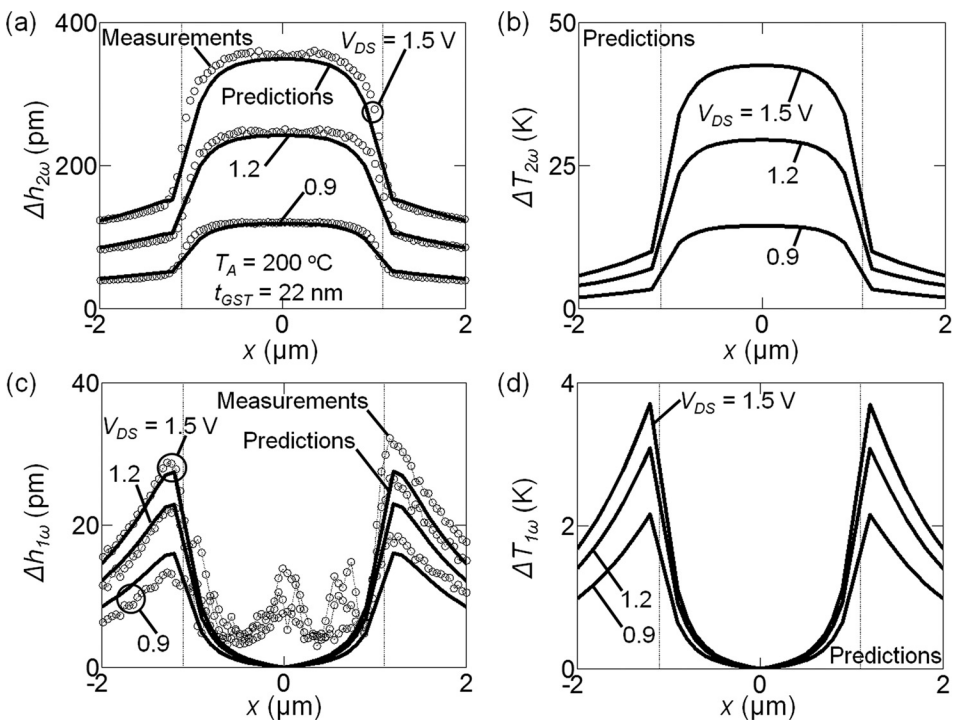

FIG. 4. Measured and predicted Δh and ΔT for a 2.2 μm channel length and 22 nm thin GST device annealed at 200 °C for $V_{DS} = 0.9$, 1.2, and 1.5 V. (a) Measured and predicted second harmonic surface expansions Δh_{2w} due to Joule heating. Black circles and solid black lines show measurements and predictions. (b) Predicted $\Delta T_{2\omega}$ from fitting measurements and predictions in (a). The model predicts $\rho_{GST} = 4.8 \pm 0.3 \times 10^{-5}$ Ω m and $\rho_C = 1.1 \pm 0.3 \times 10^{-11}$ Ω m^2. (c) Measured and predicted first harmonic surface expansions $\Delta h_{1\omega}$ due to Peltier effects. Black circles and solid black lines show measurements and predictions. (d) Predicted $\Delta T_{1\omega}$ from fitting measurements and predictions in (a). The model predicts $S_{GST} = 110 \pm 10\,\mu$V K^{-1}.

contact, Peltier heating and cooling cause a 1.6 and 3 K change in temperature, $\Delta T_{1\omega}$, compared to the Joule heating induced temperature rise, $\Delta T_{2\omega}$, of 7 and 18 K for $V_{DS} = 0.9$ and 1.5 V. Peltier effects were ~23% and ~17% of the contact temperature change for $V_{DS} = 0.9$ and 1.5 V. A constant surface expansion of ~2–3 pm is recorded across the device for 1ω and 2ω based measurements when no bias is applied, with no correlation to the device topography. Therefore, the large Δh observed when a bias is applied to the device is due to Joule heating and Peltier effects.

B. Measurements of heterogeneous Joule and thermoelectric effects

Figure 5 shows the measured heterogeneous surface expansion for three 11 nm thin GST devices with channel lengths 2.5, 3.2, and 2.5 μm annealed at 150, 200, and 250 °C. Figures 5(a)–5(c) show the measured $\Delta h_{2\omega,Norm}$ which is the measured $\Delta h_{2\omega}$ normalized by the average channel $\Delta h_{2\omega}$. The measured $\Delta h_{2\omega,Norm}$ is an indicator of local GST Joule heating. Figures 5(d)–5(f) show the measured $\Delta h_{1\omega,Norm}$ which is the measured $\Delta h_{1\omega}$ normalized by the average contact $\Delta h_{1\omega}$. Figures 5(g)–5(i) show the measured phase of the first harmonic expansion $\Theta_{1\omega}$. The measured $\Delta h_{1\omega,Norm}$ and $\Theta_{1\omega}$ are indicators of local GST Peltier effects. The devices annealed at 150, 200, and 250 °C were driven by a device bias $V_{DS} = 4.8$, 2.6, and 1.0 V. The device

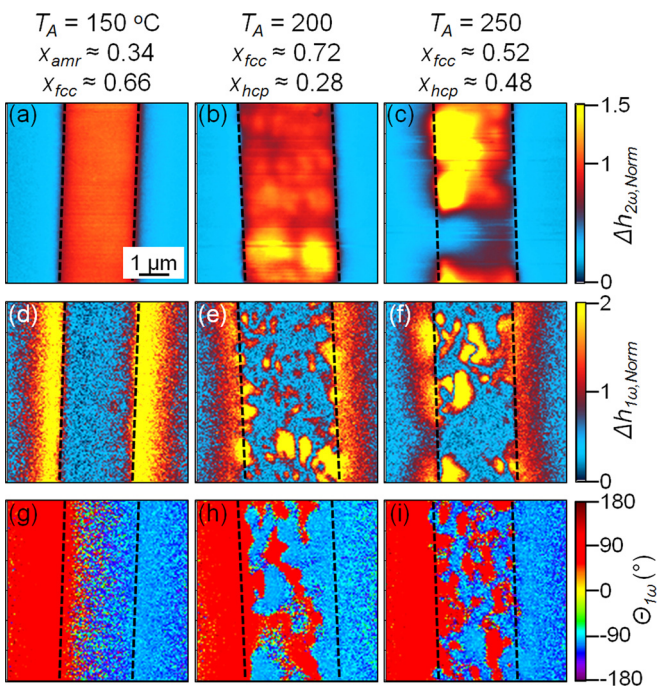

FIG. 5. Measured Δh for 11 nm thin GST devices. The devices had channel lengths of 2.5, 3.2, and 2.5 μm and were annealed at temperatures $T_A = 150$, 200, and 250 °C. The crystal fractions x_f of each device is shown. (a)–(c) Measured $\Delta h_{2\omega,Norm}$ which is the measured $\Delta h_{2\omega}$ normalized by the average channel $\Delta h_{2\omega}$, due to Joule heating. (d)–(f) Measured $\Delta h_{1\omega,Norm}$ which is the measured $\Delta h_{1\omega}$ normalized by the average contact $\Delta h_{1\omega}$, due to Peltier effects. (g)–(i) Measured $\Delta h_{1\omega}$ phase $\Theta_{1\omega}$. A 180° shift in $\Theta_{1\omega}$ distinguishes regions which experience Peltier heating from regions which experience Peltier cooling, depending on bias polarity. The $T_A = 150$ °C device is a mix of amorphous and fcc GST, and the $T_A = 200$ and 250 °C devices are a mix of fcc and hcp GST. Scale bar is shown in (a) and dashed black lines indicate the edges of the channel.

annealed at 150 °C exhibited the largest Peltier effects at the GST-TiW contacts due to the large difference in the mixed amorphous and fcc GST and TiW contact thermopower.

Figures 5(a)–5(c) show the normalized second harmonic expansion for the three devices. The measured $\Delta h_{2\omega,Norm}$ is proportional to $\Delta T_{2\omega}$ and is an indicator of local GST Joule heating. Figures 5(a)–5(c) show the heterogeneity of $\Delta h_{2\omega,Norm}$ increases with annealing temperature. We attribute the lateral heterogeneous Joule heating of our devices to the presence of large grains of hcp GST in a matrix of fcc GST. The presence of hcp grains in a matrix of fcc GST would create a non-uniform resistivity distribution causing heterogeneous lateral Joule heating. The device in Fig. 5(a) has a low hcp phase crystal fraction and experiences uniform Joule heating, and the device in Fig. 5(c) is composed of ~48% hcp GST and experiences heterogeneous Joule heating. The measured $\Delta h_{2\omega,Norm}$ deviates ~45% across the channel in Fig. 5(c), or the Joule heating induced temperature rise varies ±45% across the channel. The supplement further describes heterogeneous lateral Joule heating including a similar but smaller trend for the 22 nm thin GST samples.[26]

Figures 5(d)–5(f) show the normalized first harmonic expansion for the three devices. The measured $\Delta h_{1\omega,Norm}$ is proportional to $\Delta T_{1\omega}$ and is an indicator of local Peltier effects due to lateral changes in material thermopower. Figure 5(d) shows $\Delta h_{1\omega,Norm}$ for a device which experiences uniform Peltier effects at the contacts and no Peltier effects in the channel, indicating the channel has uniform thermopower. Figures 5(e) and 5(f) show $\Delta h_{1\omega,Norm}$ for two devices with significant hcp GST crystal fraction and show significant $\Delta h_{1\omega,Norm}$ measured in the channel. The presence of both fcc and hcp GST in the channel causes local Peltier heating and cooling due to the large difference in fcc and hcp GST thermopower (150–300 μV K^{-1}).[7,10,13] Large spikes are evident in $\Delta h_{1\omega,Norm}$ for these two devices in the channel and at the contacts. The heterogeneous resistivity distribution forms preferential current pathways, locally increasing the current density and locally enhancing thermoelectric effects.[22] However, the average $\Delta h_{1\omega}$ is the largest in Fig. 5(d) due to the large difference in amorphous-fcc GST and TiW thermopower (200–400 μV K^{-1}).[7,10,13]

Figures 5(g)–5(i) show the measured phase of the first harmonic expansion for the three devices. SJEM measures the first harmonic expansion amplitude $\Delta h_{1\omega}$ and phase $\Theta_{1\omega}$. The measured $\Delta h_{1\omega}$ indicates the magnitude of Peltier heating and cooling. The measured $\Theta_{1\omega}$ indicates if the sample experiences local Peltier heating or cooling with bias polarity. A 180° shift in $\Theta_{1\omega}$ is observed between Peltier heated and cooled locations. Figure 5(d) shows measurable $\Delta h_{1\omega}$ at the contacts indicating Peltier effects at the contacts. Figure 5(g) shows a 180° shift in $\Theta_{1\omega}$ between the contacts indicating one contact experiences Peltier heating while the other contact experiences Peltier cooling. Therefore, Peltier heating and cooling can be discerned by combination of measureable $\Delta h_{1\omega}$ and 180° shifts in $\Theta_{1\omega}$. The devices in Figs. 5(h) and 5(i) show similar behavior to Fig. 5(g), but additional peaks in $\Delta h_{1\omega}$ and 180° shifts in $\Theta_{1\omega}$ are observed in the channel corresponding to intra-GST Peltier heating and cooling, due to the presence of fcc and hcp GST.

We hypothesize why uniform lateral heating is observed in amorphous-fcc GST devices and heterogeneous lateral heating is observed in fcc-hcp GST devices. We attribute the difference in heating due to the different growth mechanisms of fcc and hcp GST which develop different grain structure. Previous work has shown fcc GST grows from amorphous GST as small grains (<10 nm) or 20–30 nm diameter columns at a GST-SiO_2 surface.[31,33] Previous work has also shown that fcc GST grows as a uniform lateral plane from amorphous GST at a free GST surface.[31] Our samples have both a GST-SiO_2 and free GST surface. The growth of a uniform lateral plane of fcc GST would result in uniform heating for amorphous-fcc samples. Also, a device composed of small (<30 nm) grains of fcc GST would exhibit homogeneous properties at the 50-nm scale, and SJEM measurements of the device would also observe uniform heating. Previous work has shown fcc GST gradually transforms into hcp GST with increasing annealing temperature.[14] We observe heterogeneous lateral heating of our fcc-hcp GST devices indicating the hcp grains increase to a size greater than the measurement spatial resolution. The observation of Peltier heating and cooling in the GST channel indicates Peltier effects between fcc and hcp GST with different thermopowers. We conclude the uniform lateral heating of amorphous-fcc GST devices is due to the planar or small grain size growth of fcc GST, and the heterogeneous lateral heating of fcc-hcp GST devices is due to the gradual growth of large hcp grains from fcc GST.

C. Predictions of heterogeneous Joule and thermoelectric effects

Figure 6 shows the measured and predicted surface thermo-mechanical expansion for a measured and simulated 22 nm thick GST device. The measured device has a channel length of 7.5 μm and was annealed at 250 °C. The simulated device has a channel length of 8 μm. We do not expect a match between measurements and predictions as the exact phase distribution of the measured device is unknown. The supplement describes the development of the FEA model used to simulate a mixed phase GST device.[26]

Figure 6(a) shows the simulated phase distribution of the GST channel. Cylinders with 400 nm diameter and 22 nm thick hcp GST were randomly placed in a matrix of fcc GST. Additional hcp GST was added at several locations to reduce meshing and computation intensity. The measured and simulated devices are composed of $70 \pm 3\%$ and 67% hcp GST. The simulated fcc and hcp GST properties were $\rho_{GST} = 2 \times 10^{-4}$ and 3.3×10^{-5} and $S_{GST} = 200$ and 15 μV K^{-1}.

Figures 6(b)–6(g) show the measured and predicted surface expansion for the two devices. Figures 6(b) and 6(c) show measured and simulated heterogeneous $\Delta h_{2\omega}$, indicating non-uniform Joule heating and resistivity distribution. The heterogeneous resistivity distribution is due to the presence of large and randomly mixed hcp GST grains in the device. Figures 6(d)–6(g) show measured and simulated spikes in $\Delta h_{1\omega}$ and 180° shifts in $\theta_{1\omega}$ indicating local Peltier effects. The Peltier effects observed at the GST-TiW contact are due to the difference in thermopower between the GST and TiW. The Peltier effects observed in the GST channel are due to the difference in thermopower between fcc and hcp GST. The simulation only considers Joule and Peltier effects in a lateral GST device due to a random mixture of large hcp and fcc GST grains with no interface resistance between the grains, and the simulation predicts the measured heterogeneous heating behavior well. Therefore, the majority of heterogeneous Joule heating in the devices is attributed to the finite resistivity of the large fcc and hcp grains.

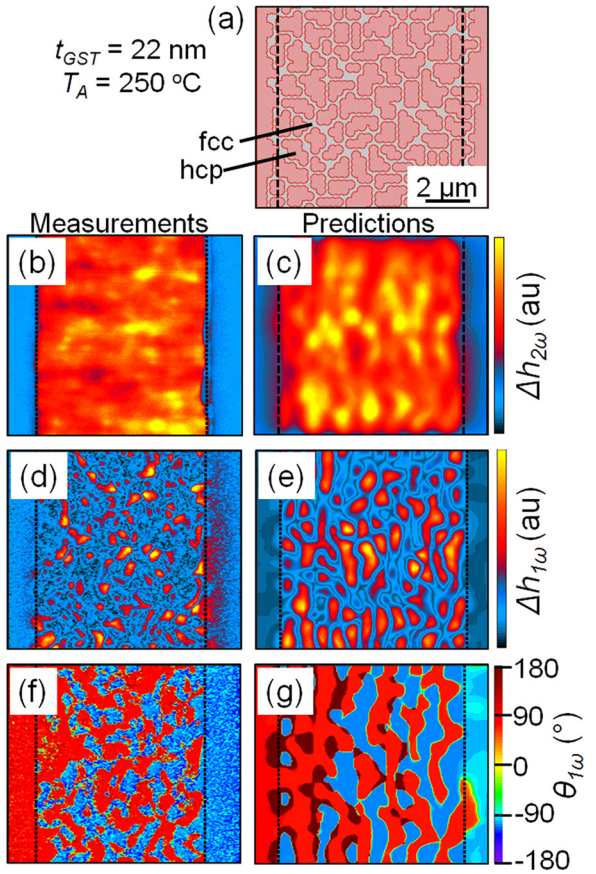

FIG. 6. Measurements (b, d, and f) and predictions (c, e, and g) of Δh for a 22 nm thin GST device. The measured device has a 7.5 μm channel length and was annealed at 250 °C. The simulated device has an 8 μm channel length. We do not expect a match between measurements and predictions as the measurement phase distribution is unknown. (a) Schematic of model phase distribution with fcc and hcp GST shown in gray and red. (b and c) Measured and predicted heterogeneous Δh_{2w} due to Joule heating of preferential current pathways through mixed fcc and hcp GST. (d and e) Measured and predicted $\Delta h_{1\omega}$ due to local Peltier effects between fcc and hcp GST and at the GST-TiW contact. (f and g) Measured and predicted $\Theta_{1\omega}$. The 180° shifts in Θ_{1w} are consistent with Peltier heating and cooling, depending on bias polarity. The dotted vertical black lines indicate the channel edge, and the scale bar is shown in (a).

We estimate the hcp GST grain size from Figures 6(a), 6(d), and 6(e). The same method is used to calculate the average hcp GST grain length l_{hcp} from Figs. 6(d) and 6(e), and the accuracy of the method is verified by comparing the calculated l_{hcp} from Figs. 6(a) and 6(e). We calculate $l_{hcp} = 0.8$ μm for the simulation from Fig. 6(a) by dividing the volume of hcp GST by the number of hcp grains and assuming the hcp GST is composed of uniform diameter cylinders which are 22 nm thick. The supplement describes the

calculation of l_{hcp} using Figs. 6(d) and 6(e),[26] briefly described here. Figures 6(d) and 6(e) are used to calculate l_{hcp} by estimating the average distance between $\Delta h_{1\omega}$ peaks, which correspond to changes in GST phase. We calculate $l_{hcp} = 1.1\ \mu$m for the device shown in Fig. 6(e), close to the $l_{hcp} = 0.8\ \mu$m from Fig. 6(a). We expect our method of calculating l_{hcp} from peaks in $\Delta h_{1\omega}$ to overestimate l_{hcp} as not every fcc-hcp interface experiences significant Peltier effects. We calculate $l_{hcp} = 0.7\ \mu$m for the device shown in Fig. 6(c) which is a 22 nm thick GST sample annealed at 250 °C.

D. GST properties from SJEM measurements

Figure 7 shows the measured and predicted surface expansion for a 3.2 μm channel length and 11 nm thin GST device annealed at 200 °C. The measured Δh was heterogeneous in the y-direction due to the non-uniform fcc and hcp phase distribution, discussed above. Matching 2D FEA predictions and SJEM measurements predicted the effective device properties. Measurements are an average of 18 line scans with deviations smaller than the markers.

Figure 7(a) shows the measured and predicted second harmonic expansion for the device at $V_{DS} = 1.5$, 2.2, and 2.6 V. Fitting the measured and predicted $\Delta h_{2\omega}$ predicts $\rho_{GST} = 5.5 \pm 0.4 \times 10^{-5}\ \Omega$ m and $\rho_C = 3.3 \pm 0.5 \times 10^{-10}\ \Omega\ \text{m}^2$, similar to TLM measurements. The supplement details the discrepancy between the measured and predicted $\Delta h_{2\omega}$ at the contacts due to error in simulating the thick PMMA coating of this device.[26]

Figure 7(b) shows the measured and predicted first harmonic expansion for the device at $V_{DS} = 2.6$ V. The other biases are not shown for clarity, but all bias conditions are used when fitting measurements and predictions. Fitting the measured and predicted $\Delta h_{1\omega}$ predicts $S_{GST} = 72 \pm 10\ \mu\text{V K}^{-1}$ for the device with a calculated composition of 72 ± 1% fcc and 28 ± 1% hcp GST. Fitting measurements and predictions for ρ_{GST}, ρ_C, and S_{GST} yields $R^2 = 0.65$. Figure 7(b) shows additional measured $\Delta h_{1\omega}$ peaks in the channel due to Peltier effects between fcc and hcp GST. The observed Peltier effects are accompanied by changes in $\Delta h_{2\omega}$, or local Joule heating. The local change in Joule and Peltier effects indicates current is flowing between fcc and hcp GST due to their different resistivities and thermopowers. Heterogeneous heating of GST was not included in the 2D FEA model.

We observe an increase in the heterogeneity of the measured expansion as the GST thickness decreases. Figures 4 and 7 show the measured Δh of two devices with similar channel lengths and annealing temperatures but different GST thickness. The thinner device in Fig. 7 shows increased heterogeneous heating compared to the device in Fig. 4. We observe an increase in lateral heterogeneous heating for all the 11 nm thin devices compared to similar 22 nm thin devices, which is detailed in the supplement.[26] Further study into the growth mechanisms of thin film GST[7,31,32] is required to understand the GST grain structure which causes the increased heterogeneous heating with decreasing GST thickness.

Figure 8(a) shows the predicted GST resistivity and GST-TiW contact resistivity from fitting FEA predictions to

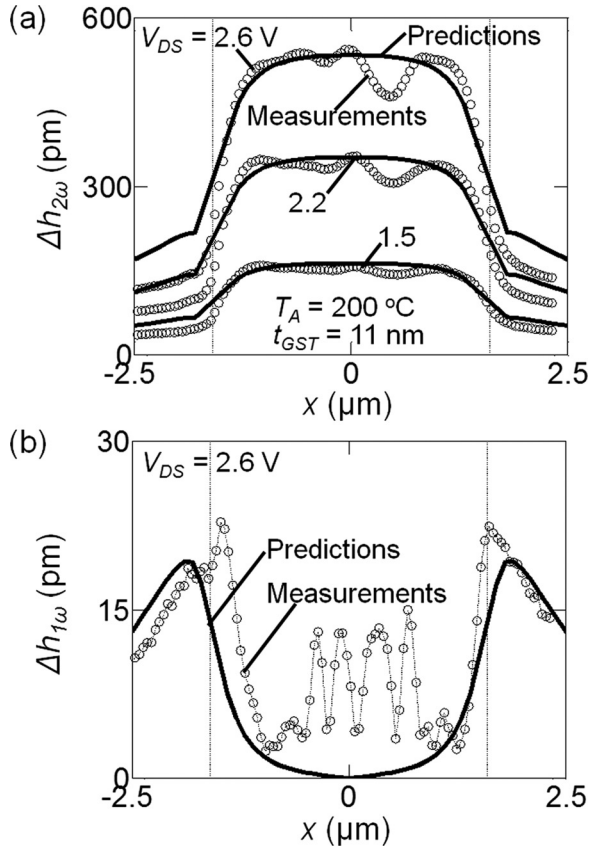

FIG. 7. Measured and predicted Δh for the 3.2 μm channel length and 11 nm thin GST device annealed at 200 °C. (a) Measured and predicted $\Delta h_{2\omega}$ for $V_{DS} = 1.5$, 2.2, and 2.6 V. Black circles and solid black lines show measurements and predictions. The model predicts the effective channel $\rho_{GST} = 5.5 \pm 0.4 \times 10^{-5}\ \Omega$ m and $\rho_C = 3.3 \pm 0.5 \times 10^{-10}\ \Omega\ \text{m}^2$, similar to TLM measurements. (b) Measured and predicted Δh_{1w} at $V_{DS} = 2.6$ V. Black circles and solid black lines show measurements and predictions. The model predicts $S_{GST} = 72 \pm 10\ \mu\text{V K}^{-1}$ for the device. Additional measured Δh_{1w} peaks in the channel center are due to Peltier effects between fcc and hcp GST, which were not included in the 2D model. The measured Δh was non-uniform in the y-direction, and the dotted vertical black lines indicate the channel edge.

SJEM measurements of $\Delta h_{2\omega}$ for all the measured devices. A minimum of 3 devices were measured per sample. The predicted ρ_{GST} in Fig. 8(a) is similar to the TLM measurements shown in Fig. 3(d). However, FEA fitting of SJEM measurements predicts lower ρ_C values than TLM measurements. The contact resistance of the 11 nm thin GST devices annealed at 250 °C and the 22 nm thin GST devices annealed at 200 and 250 °C were near the TLM measurement resolution. Therefore, TLM measurements yielded inaccurate measurements of ρ_C for these samples. However, we observed noticeable contact heating in our $\Delta h_{2\omega}$ measurements for similar devices, allowing the FEA model to predict ρ_C for these devices. Figure 8(a) shows that FEA fitting of SJEM measurements predicts lower ρ_C values for these samples than TLM measurements. FEA fitting of SJEM measurements is unable to predict $\rho_C < 2 \times 10^{-11}\ \Omega\ \mu\text{m}^2$ as no significant contact heating was observed for these devices. Adjusting the device geometry can increase the ρ_C resolution of TLM or FEA fitting of SJEM measurements.

Figure 8(b) shows the predicted GST thermopower from fitting FEA predictions to SJEM measurements of $\Delta h_{1\omega}$ for

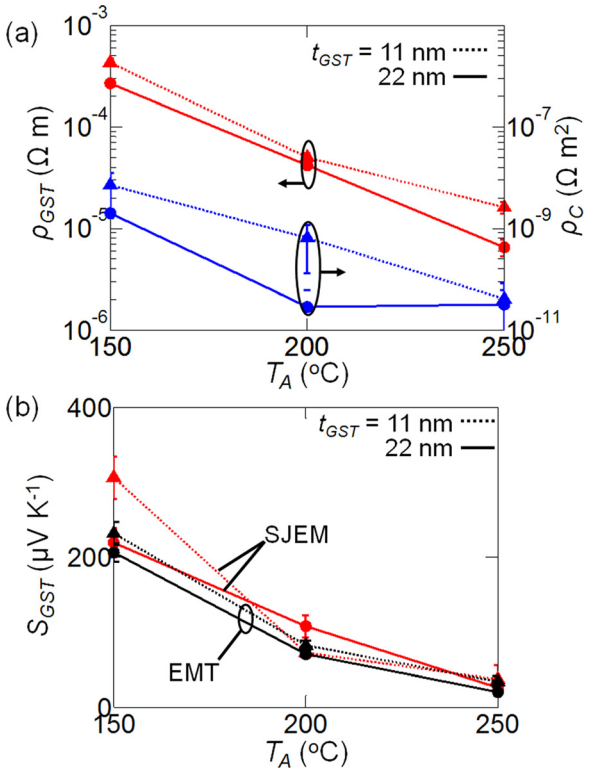

FIG. 8. Predicted GST resistivity ρ_{GST}, GST-TiW contact resistivity ρ_C, and GST thermopower S_{GST} from FEA fitting of SJEM measurements. Dotted lines with triangle markers and solid lines with circle markers show 11 and 22 nm thin GST. (a) Red and blue lines show ρ_{GST} and ρ_C. (b) Red and black lines show the predicted S_{GST} from FEA fitting of SJEM measurements and S_{GST} calculated from EMT. Error bars in (a) and (b) show the calculated standard of deviation with some deviations smaller than the markers.

all the measured devices. The GST thermopower continuously decreases with increasing annealing temperature as amorphous, fcc, and hcp GST have decreasing thermopowers. EMT was applied to calculate S_{GST} from the calculated GST crystal fractions shown in Fig. 3(b).[7,34] The supplement details the application of EMT.[26] We calculate slightly lower S_{GST} when applying EMT than the predicted S_{GST} from FEA fitting of SJEM measurements. A large discrepancy is observed between the two methods for the 11 nm thin GST sample annealed at 150 °C, and the supplement further discusses this discrepancy.[26] The agreement between EMT calculations and FEA fitting of SJEM measurements indicates EMT can accurately describe the behavior of thin film GST, and the electrical and thermoelectric properties of 11–22 nm thin GST films behave like a uniform and random mixture of bulk GST phases.[21,34]

IV. CONCLUSION

In conclusion, we measured the nanometer–scale temperature distribution and properties of lateral PCM devices with 11 and 22 nm thin GST, after annealing at 150, 200, and 250 °C. A modified SJEM technique enabled direct measurements of heterogeneous Joule and Peltier effects in thin GST films with sub-50 nm spatial and ~0.2 K temperature resolution. The GST resistivity, GST-TiW contact resistivity, and crystal fraction of each phase were estimated from TLM measurements[12] and EMT calculations.[7,21] We observe uniform heating for mixed amorphous and fcc GST and heterogeneous Joule and Peltier effects in mixed fcc and hcp GST thin films. A 3D FEA model predicts the observed heterogeneous Joule heating and Peltier effects between fcc and hcp GST and estimates the hcp grain size. Increasing the annealing temperature increases the hcp crystal fraction, increasing heterogeneous Joule and Peltier effects. Comparing SJEM measurements with a 2D FEA model predicts ρ_{GST}, ρ_C, and S_{GST} of the sub-25 nm thin GST films. The estimated S_{GST} matches well with calculations using EMT. The large measured thermopower of GST for the low annealing temperature ($T_A = 150$ °C) could reduce the energy consumption by >50% in highly scaled PCM devices due to Peltier heating, compared to scenarios which only utilize Joule heating.[9] However, higher annealing temperatures increase hcp GST crystalline fraction, which decreases GST thermopower and the predicted reduction in PCM energy consumption. Knowledge of nanometer-scale Joule, thermoelectric, and interface effects in GST devices should enable improvements in energy efficient designs of future PCM technology.

ACKNOWLEDGMENTS

The authors gratefully acknowledge support by the National Science Foundation (NSF) Grant No. ECCS 10-02026, and by the Materials Structures and Devices (MSD) Focus Center, under the Focus Center Research Program (FCRP), a Semiconductor Research Corporation entity.

[1]M. H. R. Lankhorst, B. W. S. M. M. Ketelaars, and R. A. M. Wolters, Nature Mater. **4**, 347 (2005).
[2]D. Loke, T. H. Lee, W. J. Wang, L. P. Shi, R. Zhao, Y. C. Yeo, T. C. Chong, and S. R. Elliott, Science **336**, 1566 (2012).
[3]F. Xiong, M.-H. Bae, Y. Dai, A. D. Liao, A. Behnam, E. A. Carrion, S. Hong, D. Ielmini, and E. Pop, Nano Lett. **13**, 464 (2013).
[4]F. Xiong, A. D. Liao, D. Estrada, and E. Pop, Science **332**, 568 (2011).
[5]G. W. Burr, M. J. Breitwisch, M. Franceschini, D. Garetto, K. Gopalakrishnan, B. Jackson, B. Kurdi, C. Lam, L. A. Lastras, A. Padilla, B. Rajendran, S. Raoux, and R. S. Shenoy, J. Vac. Sci. Technol. B **28**, 223 (2010).
[6]D.-S. Suh, C. Kim, K. H. P. Kim, Y.-S. Kang, T.-Y. Lee, Y. Khang, T. S. Park, Y.-G. Yoon, J. Im, and J. Ihm, Appl. Phys. Lett. **96**, 123115 (2010).
[7]J. Lee, T. Kodama, Y. Won, M. Asheghi, and K. E. Goodson, J. Appl. Phys. **112**, 014902 (2012).
[8]D. T. Castro, L. Goux, G. A. M. Hurkx, K. Attenborough, R. Delhougne, J. Lisoni, F. J. Jedema, M. A. A. 't Zandt, R. A. M. Wolters, D. J. Gravesteijn, M. Verheijen, M. Kaiser, and R. G. R. Weemaes, in *IEEE International Electron Devices Meeting, San Francisco, CA, USA, 10–12 December* (2007), pp. 315–318.
[9]J. Lee, M. Asheghi, and K. E. Goodson, Nanotechnology **23**, 205201 (2012).
[10]T. Kato and K. Tanaka, Jpn. J. Appl. Phys., Part 1 **44**, 7340 (2005).
[11]J. D. Koenig, H. Boettner, J. Tomforde, and W. Bensch, in *26th International Conference on Thermoelectrics, 3–7 June* (2007), pp. 390–393.
[12]K. L. Grosse, F. Xiong, S. Hong, W. P. King, and E. Pop, Appl. Phys. Lett. **102**, 193503 (2013).
[13]E. Bozorg-Grayeli, J. P. Reifenberg, M. Asheghi, H.-S. P. Wong, and K. E. Goodson, in *Annual Review of Heat Transfer*, edited by G. Chen, V. Prasad, and Y. Jaluria (Begell House, 2013), Vol. 16, pp. 397.
[14]H.-K. Lyeo, D. G. Cahill, B.-S. Lee, J. R. Abelson, M.-H. Kwon, K.-B. Kim, S. G. Bishop, and B.-k. Cheong, Appl. Phys. Lett. **89**, 151904 (2006).
[15]S. Raoux, J. L. Jordan-Sweet, and A. J. Kellock, J. Appl. Phys. **103**, 114310 (2008).

[16]X. Wei, L. Shi, T. C. Chong, R. Zhao, L. Koon, and H. Koon, Jpn. J. Appl. Phys. **46**, 2211 (2007).
[17]D. L. Kencke, I. V. Karpov, B. G. Johnson, S. J. Lee, D. Kau, S. J. Hudgens, J. P. Reifenberg, S. D. Savransky, J. Zhang, M. D. Giles, and G. Spadini, in *IEEE International Electron Devices Meeting, 10–12 December* (2007), pp. 323–326.
[18]J. P. Reifenberg, D. L. Kencke, and K. E. Goodson, IEEE Electron Device Lett. **29**, 1112 (2008).
[19]F. Xiong, A. Liao, and E. Pop, Appl. Phys. Lett. **95**, 243103 (2009).
[20]I. R. Chen and E. Pop, IEEE Trans. Electron Devices **56**, 1523 (2009).
[21]R. Landauer, J. Appl. Phys. **23**, 779 (1952).
[22]K. L. Grosse, M.-H. Bae, F. Lian, E. Pop, and W. P. King, Nat. Nanotechnol. **6**, 287 (2011).
[23]J. Varesi and A. Majumdar, Appl. Phys. Lett. **72**, 37 (1998).
[24]X. Xie, K. L. Grosse, J. Song, C. Lu, S. Dunham, F. Du, A. E. Islam, Y. Li, Y. Zhang, E. Pop, Y. Huang, W. P. King, and J. A. Rogers, ACS Nano **6**, 10267 (2012).
[25]S. P. Gurrum, W. P. King, Y. K. Joshi, and K. Ramakrishna, J. Heat Transfer **130**, 082403 (2008).
[26]See supplementary material at http://dx.doi.org/10.1063/1.4896492 for *in-situ* annealing resistance measurements, TLM measurements, EMT calculations, FEA model information, hetergenous sample heating trends, and hcp grain size calculations.
[27]E. M. Lifshitz, L. D. Landau, and L. P. Pitaevskii, *Electrodynamics of Continuous Media* (Butterworth-Heinemann, 1984).
[28]J. Martin, in *The COMSOL Conference*, Hannover, Germany, 4–6 November (2008), pp. 1–7.
[29]F. J. DiSalvo, Science **285**, 703 (1999).
[30]D. K. Schroder, *Semiconductor Material and Device Characterization* (Wiley Interscience, 2006).
[31]S. Lombardo, E. Rimini, M. G. Grimaldi, and S. Privitera, Microelectron. Eng. **87**, 294 (2010).
[32]H. K. Peng, K. Cil, A. Gokirmak, G. Bakan, Y. Zhu, C. S. Lai, C. H. Lam, and H. Silva, Thin Solid Films **520**, 2976 (2012).
[33]J. Lee, Z. Li, J. P. Reifenberg, S. Lee, R. Sinclair, M. Asheghi, and K. E. Goodson, J. Appl. Phys. **109**, 084902 (2011).
[34]J. Sonntag, Phys. Rev. B **73**, 045126 (2006).
[35]K. L. Grosse, E. Pop, and W. P. King, Rev. Sci. Instrum. **85**, 094904 (2014).

Supporting Online Materials for

"Heterogeneous nanometer-scale Joule and Peltier effects in sub-25 nm thin phase change memory devices"

By: Kyle L. Grosse, E. Pop, and William P. King
University of Illinois at Urbana-Champaign, Urbana, Illinois 61801, USA

I. *In-situ* Annealing Resistance Measurements

The sample resistance was measured during the anneal using contacts patterned at the corners of each sample. Before sputtering the GST, we patterned and sputtered TiW contacts at the corners of each sample to contact the GST and measure the GST sample resistance R_{Sample} while annealing. The GST was then sputtered on top of the sample. The samples were annealed in a N_2 environment at temperatures T_A = 150, 200, or 250 °C for 10 min, with a heating and cooling rate of ~30 °C min^{-1}. After annealing, we patterned and sputtered TiW/Au contacts to form the lateral GST devices.

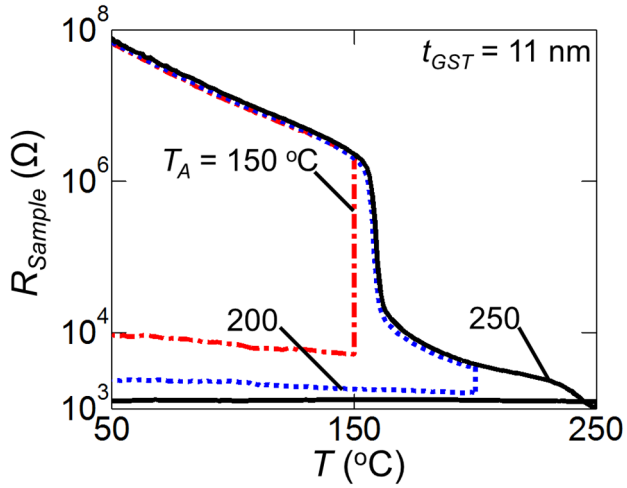

FIG. S1. *In-situ* annealing sample resistance R_{Sample} with temperature T. The GST samples were 11 nm thin and annealed at temperatures T_A = 150, 200, and 250 °C shown in dash-dot red, dotted blue, and solid black lines. Samples were annealed in N_2 environment at T_A for 10 min with 30 °C min^{-1} heating and cooling rate.

Figure S1 shows *in-situ* annealing R_{Sample} measurements for the 11 nm thin GST samples annealed at 150, 200, and 250 °C. The measurements are two probe resistance measurements across the ~1.5 × 1.5 cm^2 samples. The large change in R_{sample} at ~160 °C indicates the majority of GST quickly transforms from amorphous to fcc GST.[1,2] Although the sample annealed at 150 °C was below the transition temperature, the measured ~10^4 Ω change in room temperature resistance indicates the sample is predominately fcc phase GST. Samples annealed at higher temperatures have >10^4 Ω change in resistance, indicating the presence of hcp GST.[3]

II. Transfer Length Method Measurements

Figure S2 shows transfer length method (TLM) measurements of all samples. The lateral GST devices have a device width W = 245 μm and a channel length (source-drain spacing) L = 2-12 μm. The calculation of GST resistivity ρ_{GST} and GST-TiW contact resistivity ρ_C from TLM measurements[4,5] is discussed below for the 11 nm thin GST sample annealed at 150 °C, shown in Fig. S2(a). Simple linear regression of device resistance R_{DS} yields the sheet resistance $R_{\square}$ = 37 ± 2 kΩ/□ (ρ_{GST} = 4.1 ± 0.2×10^{-4} Ω m) and twice the contact resistance per width $2R_C \times W$ = 42 ± 15 kΩ μm with a coefficient of determination R^2 = 0.97 for the fit. The current transfer length L_T and ρ_C are calculated from:[6]

$$R_C \times W = (\rho_C / L_T)\coth(L_C / L_T) \tag{S1}$$

$$L_T = \sqrt{\rho_C / R_{\square}} \ . \tag{S2}$$

Equations S1 and S2 yield ρ_C = 1.2 ± 0.9×10^{-8} Ω m^2 and L_T = 570 ± 210 nm for the 11 nm thin GST sample annealed at 150 °C. We note L_T is much smaller than the TiW contact length L_{CON}.[5] Some of the devices for the 11 nm thin GST sample annealed at 150 °C had partially destroyed channels, and W was measured optically for each device on this sample. All other samples had intact channels.

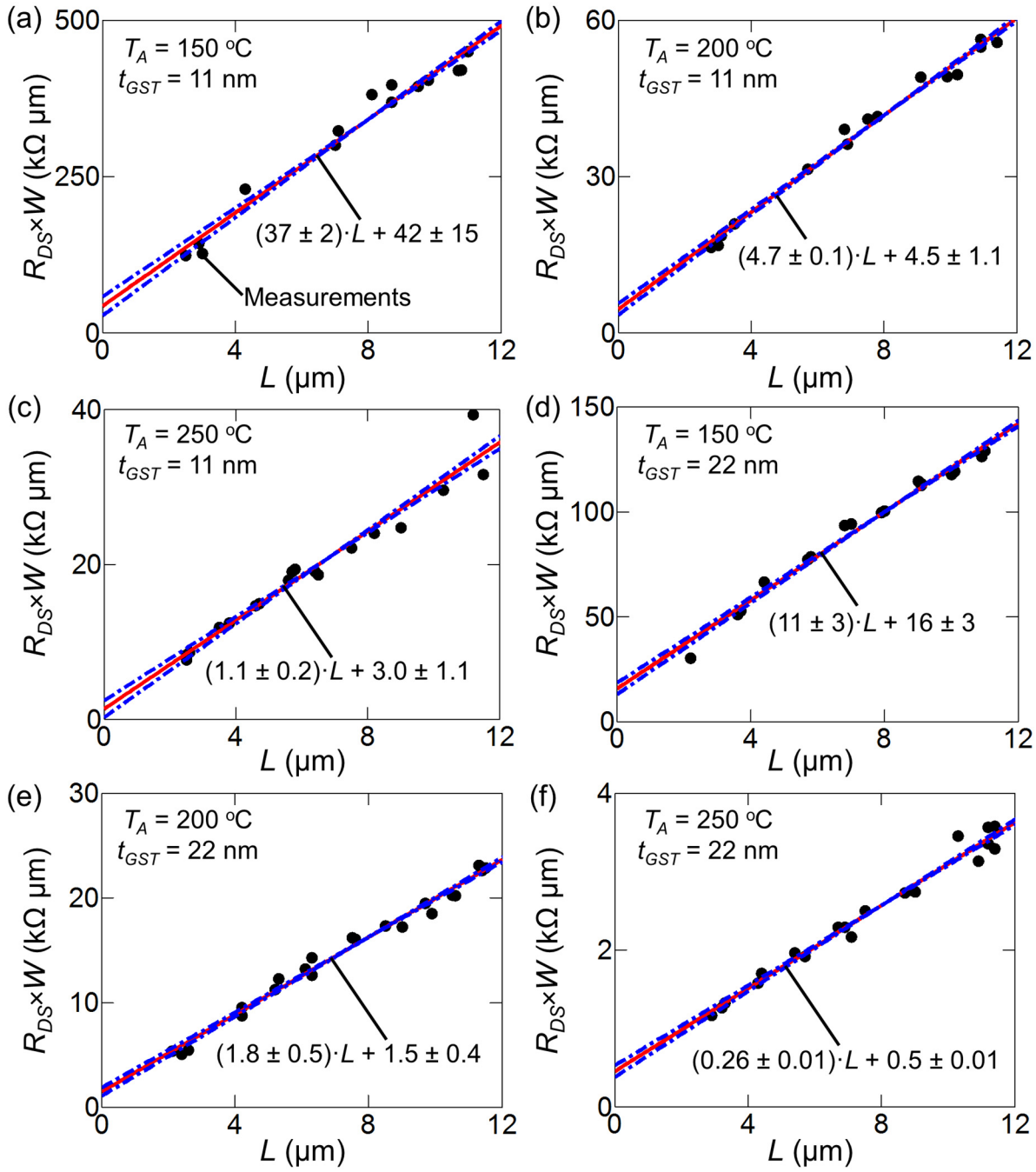

FIG. S2. Transfer length method (TLM) measurements of all samples. The GST thickness t_{GST} and annealing temperature T_A are labeled on each plot. The black dots are measurements. The solid red and dash-dot blue lines are the simple linear regression best fit and deviation. The slope of the fit is the sheet resistance $R_{\square}$ in kΩ/□ and the y-axis intercept is twice the contact resistance per width $2R_C \times W$ in kΩ μm.

III. Effective Media Theory

A. Calculated Crystal Fractions

Effective media theory[7] (EMT) was applied to calculate the crystal fraction of each sample. EMT predicts the effective properties of a multiple phase mixture assuming each phase is randomly distributed as spheres in a uniform effective medium.[7] The main text describes the assumption that each sample is a binary phase mixture. We assume the samples annealed at 150 °C are a mixture of amorphous and fcc GST and samples annealed above 150 °C are a mixture of fcc and hcp GST. Equation S3 relates the crystal fraction x_f and conductivity σ of a binary mixture composed of A and B phases.[7]

$$x_A \frac{\sigma_A - \sigma_E}{\sigma_A + 2\sigma_E} + x_B \frac{\sigma_B - \sigma_E}{\sigma_B + 2\sigma_E} = 0 \qquad \text{(S3)}$$

The subscripts denote the material phase, and the effective mixture conductivity is given by σ_E. TLM measurements yielded the effective resistivity of each sample. The crystal fraction is calculated using Eq. S3, using the measured ρ_{GST}, and assuming the resistivity of amorphous, fcc, and hcp GST are ρ_{amr} = 1 Ω m, $\rho_{fcc} = 2\times10^{-4}$ Ω m, and $\rho_{hcp} = 3.3\times10^{-6}$ Ω m, similar to published values.[3,8] Equation S3 can also calculate the effective thermal conductivity of a binary mixture. Standard linear regression was used to find the average and deviation of the estimated GST resistivity and GST-TiW contact resistivity from TLM measurements. The assumed normal distribution of these properties were used in all calculations using EMT to estimate the GST crystal fractions and GST thermopower.

B. Calculated GST Thermopower

EMT was applied to calculate the thermopower[9,10] of the samples. Equation S4 relates the thermal conductivity k and thermopower S of a binary mixture of A and B phases.

$$\frac{k_E}{S_E} = \frac{1}{4}\left\{(3x_A - 1)\frac{k_A}{S_A} + (3x_B - 1)\frac{k_B}{S_B} + \left[\left((3x_A - 1)\frac{k_A}{S_A} + (3x_B - 1)\frac{k_B}{S_B}\right)^2 + 8\frac{k_A}{S_A}\frac{k_B}{S_B}\right]^{\left(\frac{1}{2}\right)}\right\} \quad \text{(S4)}$$

The subscripts denote the material phase, and the effective mixture thermal conductivity and thermopower are given by k_E and S_E. The effective thermopower is calculated using Eq. S4, the calculated crystal fractions, and assuming the thermal conductivity and thermopower of amorphous, fcc, and hcp GST are k_{amr} = 0.2 W m^{-1} K^{-1}and S_{amr} = 400 μV K^{-1}, k_{fcc} = 0.6 W m^{-1} K^{-1} and S_{fcc} = 200 μV K^{-1}, and k_{hcp} = 1.7 W m^{-1} K^{-1} and S_{hcp} = 15 μV K^{-1}, similar to published values.[3,9,11] Equation S3 was used to calculate the effective thermal conductivity for each sample.

C. Calculated Thermopower Discrepancy

Three factors may explain the discrepancy between the thermopower calculated applying EMT and the thermopower predicted by FEA fitting of SJEM measurements for the 11 nm thin GST sample annealed at 150 °C. (1) Amorphous GST thermopower is larger than the value used in our EMT calculations. Increasing the amorphous GST thermopower in our calculations would improve the fit between the EMT calculated and FEA predicted thermopower for the 11 nm thin GST sample annealed at 150 °C. However, increasing the amorphous GST thermopower in our calculations would also worsen the fit between the EMT calculated and FEA predicted thermopower for the 22 nm thin GST sample annealed at 150 °C. (2) Amorphous GST thermopower increases as the GST thickness decreases to 11 nm. Therefore, only the EMT calculated thermopower of the 11 nm thin sample annealed at 150 °C would increase. However, the mean free path of carriers in amorphous GST is less than a few nanometers,[12] and amorphous GST thermopower should be similar to bulk values for GST films thicker than 10 nm. Previous work has shown no dependence of amorphous GST thermopower with GST film thickness down

to 25 nm.[9] (3) Thermoelectric transport for the 11 nm thin GST sample annealed at 150 °C is dominated by amorphous GST. The FEA predicted GST thermopower for this sample is close to amorphous GST thermopower, indicating the amorphous phase may dominate thermoelectric effects in such thin GST films. However, we would also expect amorphous GST to dominate the measured GST resistivity for the same sample. Further work is required to explain the discrepancy between the thermopower calculated applying EMT and the thermopower predicted by FEA fitting of SJEM measurements for the 11 nm thin GST sample annealed at 150 °C.

IV. Finite Element Analysis Model

A. Model Implementation

Two and three dimensional (2D and 3D) frequency domain thermoelectric-mechanical finite element analysis (FEA) models were developed in COMSOL to predict GST device behavior. Fitting the 2D model to SJEM measurements predicted device properties, temperature rise ΔT, and surface thermo-mechanical expansion Δh. The 3D FEA model was used to explain heterogeneous device heating. The derivation of FEA models for similar devices has been previously described[5] and is briefly described below.

The thermo-mechanical expansion Δh and corresponding temperature rise ΔT were predicted from a FEA model of the devices, used to interpret the SJEM measurements. Equations S5 and S6 show the modified heat diffusion and Poisson equations to account for thermoelectric transport.[13,14]

$$\rho_d c_P \frac{\partial T}{\partial t} = \nabla(k + \sigma S^2 T)\nabla T + \nabla(\sigma S T)\nabla V + \sigma(S\nabla T\nabla V + [\nabla V]^2) \quad \text{(S5)}$$

$$\nabla\sigma(S\nabla T + \nabla V) = 0 \quad \text{(S6)}$$

The density, heat capacity, thermal conductivity, electrical conductivity, thermopower, temperature, and voltage are given by ρ_d, c_P, k, σ, S, T, and V. The Fourier transform of Eqs. S5 and S6 for sinusoidal voltage and temperature fields yield Eq. S7.

$$\nabla\begin{bmatrix} 4(k+\sigma S^2 T_{0\omega}) & 2\sigma S^2 T_{1\omega} & 2\sigma S^2 T_{2\omega} & 4\sigma S T_{0\omega} & 2\sigma S T_{1\omega} \\ 2\sigma S^2 T_{1\omega} & 2k+\sigma S^2(2T_{0\omega}+T_{2\omega}) & \sigma S^2 T_{1\omega} & 2\sigma S T_{1\omega} & \sigma S(2T_{0\omega}+T_{2\omega}) \\ 2\sigma S^2 T_{2\omega} & \sigma S^2 T_{1\omega} & 2(k+\sigma S^2 T_{0\omega}) & 2\sigma S T_{2\omega} & \sigma S T_{1\omega} \\ \sigma S & 0 & 0 & \sigma & 0 \\ 0 & \sigma S & 0 & 0 & \sigma \end{bmatrix}\nabla\begin{bmatrix} T_{0\omega} \\ T_{1\omega} \\ T_{2\omega} \\ V_{0\omega} \\ V_{1\omega} \end{bmatrix} = \ldots - \begin{bmatrix} 2\sigma\left\{S(2\nabla T_{0\omega}\nabla V_{0\omega}+\nabla T_{1\omega}\nabla V_{1\omega})+2(\nabla V_{0\omega})^2+(\nabla V_{1\omega})^2\right\} \\ \sigma\left\{S(2\nabla T_{0\omega}\nabla V_{1\omega}+2\nabla T_{1\omega}\nabla V_{0\omega}+\nabla T_{2\omega}\nabla V_{1\omega})+4\nabla V_{1\omega}\nabla V_{0\omega}\right\}-i4\pi\rho_d c_P T_{1\omega}\omega \\ \sigma\left\{S(\nabla T_{1\omega}\nabla V_{1\omega}+2\nabla T_{2\omega}\nabla V_{0\omega})+(\nabla V_{1\omega})^2\right\}-i4\pi\rho_d c_P T_{2\omega}2\omega \\ 0 \\ 0 \end{bmatrix} \quad \text{(S7)}$$

The subscripts denote the amplitude of V and T at the zero, first, and second harmonics (0ω, 1ω, and 2ω). Equation S7 was coded into the PDE physics module of COMSOL to predict device thermoelectric behavior and coupled with thermo-mechanical physics in COMSOL to estimate the frequency response of the predicted Δh and ΔT. The COMSOL model predicts Peltier effects occur at all interfaces between different thermopower materials which experience significant current flow.[14] The model predicts current only flows between the GST and TiW domains. Therefore, the model accounts for Peltier effects between all GST-TiW and fcc-hcp phase GST interfaces. All three materials are present in the 3D model, and the 3D model predicts Peltier effects between all these materials. The 2D model approximates the mixed fcc-hcp phase GST as a uniform media with effective properties and does not account for Peltier effects between fcc-hcp GST. Interface resistance and dissipation were implemented in COMSOL using home-built code.

The 2D and 3D FEA models are similar to our previous FEA model[5] with modified electrode properties, large thermal interface conductances, and accounting for non-uniform channel power dissipation. We set the electrode resistivity to zero for the current model. Therefore, the predicted resistance of the FEA model was equal to the predicted device resistance as the model did not predict the additional electrode resistance. The density, heat capacity, coefficient of thermo-mechanical expansion, Poisson's ratio, and elastic modulus of the Au/TiW electrodes were 1,900 kg m^{-3}, 129 J kg^{-1} K^{-1}, 12×10^{-6} K^{-1}, 0.42, and 80 GPa. The measured resistivity of our Au/TiW contacts was used with the Wiedemann-Franz law to calculate the thermal conductivity of our electrodes to be ~60 W m^{-1} K^{-1}. The thermal interface conductance of all interfaces was set to 10^{10} W m^{-2} K^{-1} which improved the agreement between measurements and predictions. The predicted device surface expansion of the 2D FEA model was adjusted by ±10 % to account for changes in power dissipation across the 245 μm wide channel due to variations in channel length and GST phase distribution.

B. Two and Three Dimensional Models

Figure S3 shows a schematic of the 2D FEA model. The model geometry was similar to experiments with 60-200 nm of poly(methyl methacrylate) (PMMA), 40-70 nm of Au/TiW, 11-22 nm GST, 300 nm SiO_2, and 200 μm Si, from top to bottom. The model is 400 μm wide. The large domain was chosen to be larger than the Si thermal diffusion length for the bias frequency ω = 43 kHz used in this study.[5] The device is biased at the contacts and has a heat sink at the bottom. The top surfaces are not mechanically constrained. All other surfaces are electrically and thermally insulated and mechanically constrained.

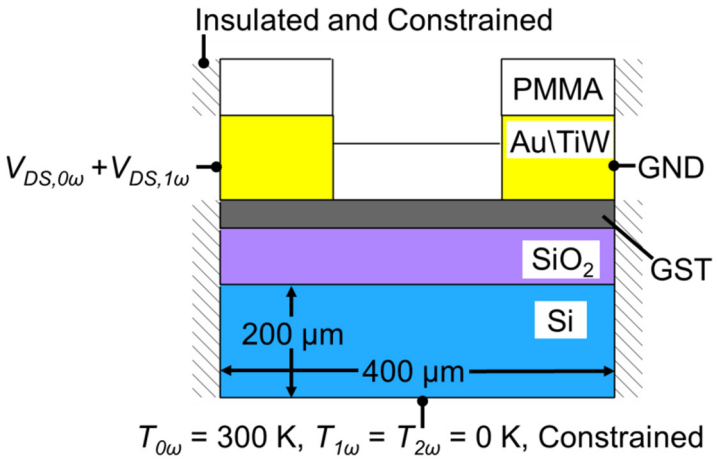

FIG. S3. Schematic of two dimensional (2D) model geometry with boundary conditions. The frequency domain zero and first harmonic device bias are given by $V_{DS,0\omega}$ and $V_{DS,1\omega}$, where $V_{DS,1\omega}$ is a complex number. The frequency domain zero, first, and second harmonic temperature rise are given by $T_{0\omega}$, $T_{1\omega}$, and $T_{2\omega}$, where $T_{1\omega}$ and $T_{2\omega}$ are complex numbers.

A 3D FEA model was developed to predict the behavior of mixed fcc and hcp GST devices. The 3D model accounts for heat spreading into the substrate and the heterogeneous lateral fcc and hcp GST distribution. The model is similar to the 2D model except the Si domain is 100 μm long in the x and z directions, and the model is 10 μm wide in the y direction. Figure 1(b) shows the axes orientations. The small model width does not significantly affect the predicted ΔT and Δh as the majority of heat transfer occurs in the x and z directions. The model has the same constraints as the 2D model. The faces normal to the y direction are electrically and thermally insulated and free to move in the z direction.

C. Calculated Device Bias and Resistance

The applied voltage amplitude V and device voltage amplitude V_{DS} are related by Equation S8.

$$V_{DS} = (V \times R_{DS}) / R \tag{S8}$$

The measured resistance is given by $R = R_{Series} + R_{DS}$, where R_{DS} is the device resistance and R_{Series} is the parasitic series resistance. Devices used for TLM measurements were also used for SJEM measurements, and the TLM measured R_{DS} was used to calculate V_{DS} for fitting FEA predictions to SJEM measurements. We subtracted a small (~5-10 Ω) parasitic resistance, due to the probes and contact pads, from the TLM measured resistance to obtain R_{DS}. The parasitic resistance was measured by contacting probes across the same contact pad. A home-built atomic force microscopy (AFM) probe station electrically contacted devices for SJEM measurements. The AFM probe station made poor contact with devices due to the PMMA coating and scratching of the soft contacts. The AFM probe station had ~10-30 Ω of parasitic series resistance. The R_{DS} predicted from FEA fitting of SJEM measurements was in good agreement with TLM measurements for all devices.

D. Thick PMMA Error

Thick layers of PMMA (>100 nm) caused a discrepancy between FEA predictions and SJEM measurements of Δh at the contacts. The measured PMMA coating is 10-20 nm thinner at the contact edge and gradually increases over a ~1 μm distance to the measured thickness. Figure S3 shows the model assumes a flat and uniform PMMA profile at the contacts. Therefore, the model has a thicker PMMA coating at the contact edge and over predicts Δh at the contact edge by ~10 %. The predicted GST-TiW contact resistivity from FEA fitting of SJEM measurements typically has >10 % error and is not significantly affected by the over prediction of Δh. However, the predicted GST thermopower from FEA fitting of SJEM measurements is over estimated by ~10% due to the over prediction of Δh at the contacts. Therefore, we decrease S_{GST} by 10 % for thick PMMA devices.

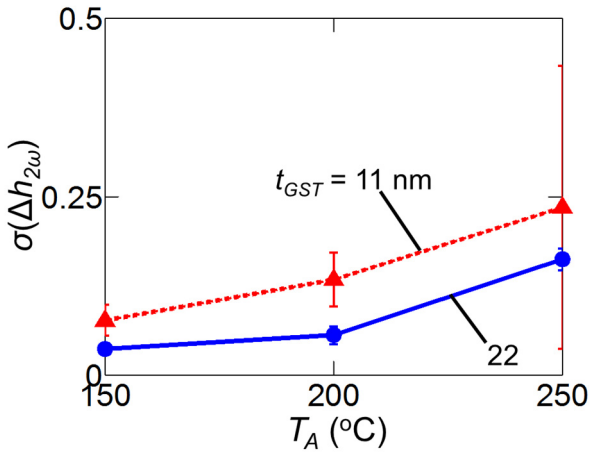

FIG. S4. Normalized deviation of $\Delta h_{2\omega}$ across the device channel $\sigma(\Delta h_{2\omega})$; calculated by dividing the deviation of $\Delta h_{2\omega}$ across the channel with the average channel $\Delta h_{2\omega}$. The measured $\sigma(\Delta h_{2\omega})$ indicates the amount of heterogeneous device Joule heating. Dashed red line with triangles and solid blue line with circle markers and show t_{GST} = 11 and 22 nm. Error bars show measurement deviation, with some error bars smaller than the markers.

V. Heterogeneous Device Heating

Figure S4 shows the normalized deviation of the measured channel second harmonic expansion $\sigma(\Delta h_{2\omega})$ for all devices. We calculate $\sigma(\Delta h_{2\omega})$ by normalizing the measured deviation of $\Delta h_{2\omega}$ across the channel with the average channel $\Delta h_{2\omega}$. The normalized deviation is a relative measure of lateral heterogeneous device Joule heating. Figure S4 shows $\sigma(\Delta h_{2\omega})$ increases with increasing annealing temperature. The main text describes the increase in lateral heterogeneous heating with increased annealing temperature due to increasing hcp GST crystal fraction. Figure S4 also shows $\sigma(\Delta h_{2\omega})$ increases with decreasing GST thickness. The increase in lateral GST heterogeneous heating with decreasing GST thickness is not well understood, and further work investigating the growth and structure of thin GST films is required to explain the trend.[1,2,9] We also observe the measured $\sigma(\Delta h_{2\omega})$ typically increases with decreasing channel length for devices with significant hcp GST crystal fraction. Decreasing channel lengths can approach the hcp grain

size and creates highly preferential current pathways, or shorts, across the device through the hcp grains. We measured similar channel length devices on each sample.

VI. Estimated hcp Grain Size

We estimated the hcp GST grain size from the measured and predicted Peltier effects shown in Figures 6(d) and (e). The data of Figs. 6(d) and (e) were mapped to a rectangular grid of points with 50 nm spacing between points. We removed all points with values less than 1.5x the average $\Delta h_{1\omega}$. We then performed the following calculation at each point. For a given point, we calculated the distance to the nearest data point in 10 ° increments. We discarded distance measurements between adjacent points indicating they were from the same $\Delta h_{1\omega}$ peak. Figures 6(d) and (e) show many of the $\Delta h_{1\omega}$ peaks are >100 nm wide and would compose many adjacent points of our grid. All the calculated distances for all the points were averaged together to find the mean distance between $\Delta h_{1\omega}$ peaks. The mean distance between $\Delta h_{1\omega}$ peaks is the average distance between fcc and hcp phases. The average fcc and hcp grain sizes determine the average distance between fcc and hcp phases, and the relative size of fcc and hcp grains can be estimated from the fcc and hcp crystal fractions. We estimated the average hcp grain size l_{hcp} by multiplying the calculated average distance between fcc and hcp phases by $2\times x_{hcp}$. We expect to overestimate l_{hcp} because not every fcc-hcp boundary caused a large local increase in $\Delta h_{1\omega}$.

Supplemental References

1 H. K. Peng, K. Cil, A. Gokirmak, G. Bakan, Y. Zhu, C. S. Lai, C. H. Lam, and H. Silva, Thin Solid Films **520**, 2976 (2012).

2 S. Lombardo, E. Rimini, M. G. Grimaldi, and S. Privitera, Microelectron. Eng. **87**, 294 (2010).

3 E. Bozorg-Grayeli, J. P. Reifenberg, M. Asheghi, H.-S. P. Wong, and K. E. Goodson, in *Annual Review of Heat Transfer*, edited by G. Chen, V. Prasad, and Y. Jaluria (Begell House, 2013), Vol. 16, pp. 397.

4 K. L. Grosse, M.-H. Bae, F. Lian, E. Pop, and W. P. King, Nature Nanotech. **6**, 287 (2011).

5 K. L. Grosse, F. Xiong, S. Hong, W. P. King, and E. Pop, Appl. Phys. Lett. **102**, 193503 (2013).

6 D. K. Schroder, *Semiconductor Material and Device Characterization*. (Wiley Interscience, 2006).

7 R. Landauer, J. Appl. Phys. **23**, 779 (1952).

8 F. Xiong, A. D. Liao, D. Estrada, and E. Pop, Science **332**, 568 (2011).

9 J. Lee, T. Kodama, Y. Won, M. Asheghi, and K. E. Goodson, J. Appl. Phys. **112**, 014902 (2012).

10 J. Sonntag, Phys. Rev. B **73**, 045126 (2006).

11 H.-K. Lyeo, D. G. Cahill, B.-S. Lee, J. R. Abelson, M.-H. Kwon, K.-B. Kim, S. G. Bishop, and B.-k. Cheong, Appl. Phys. Lett. **89**, 151904 (2006).

12 M. Nardone, M. Simon, I. V. Karpov, and V. G. Karpov, J. Appl. Phys. **112** (2012).

13 E. M. Lifshitz, L. D. Landau, and L. P. Pitaevskii, *Electrodynamics of Continuous Media*. (Butterworth-Heinemann, 1984).

14 J. Martin, in *the COMSOL Conference*, Hannover, Germany, 4-6 November, 2008, pp. 1-7.